An Efficient Earth Magnetic Field MEMS Sensor: Modeling, Experimental Results, and Optimization

Mehrdad Bagherinia, Matteo Bruggi, Alberto Corigliano, *Member, IEEE*, Stefano Mariani, David A. Horsley, *Member, IEEE*, Mo Li, and Ernesto Lasalandra

I. Introduction

THIS PAPER gives a complete description of the work briefly presented in [1].

Consumer products have recently started incorporating micro-magnetometers to be used as compasses. In combination with pressure sensors, accelerometers and gyroscopes, these sensors allow improved navigation both in scenarios where GPS is available and when it is not, such as for indoor navigation. In some cases this trend has already suggested the commercialization of multi-axis (or combo) MEMS sensor units.

Lorentz force MEMS magnetometers [2]–[9] can be particularly advantageous with respect to other devices for the measurement of magnetic fields in the direction orthogonal to the substrate (z-axis magnetometers). When compared to Hall-effect sensors, Lorentz force devices have the advantage of lower power consumption and easier integration with standard, silicon-based, MEMS fabrication technologies.

Manuscript received April 24, 2014; revised July 18, 2014; accepted July 24, 2014. The work of M. Bagherinia, M. Bruggi, A. Corigliano, and S. Mariani was supported by the Eniac Joint Undertaking Project Lab4MEMS under Grant 325622. The work of D. A. Horsley and M. Li was supported by the U.S. National Science Foundation under Award CMMI-0846379. Subject Editor R. T. Howe.

M. Bagherinia, M. Bruggi, A. Corigliano, and S. Mariani are with the Department of Civil and Environmental Engineering, Politecnico di Milano, Milan 20133, Italy (e-mail: mehrdad.bagherinia@polimi.it; matteo.bruggi@polimi.it; alberto.corigliano@polimi.it; stefano.mariani@polimi.it).

D. A. Horsley is with the Department of Mechanical and Aerospace Engineering, University of California at Davis, Davis, CA 95616 USA (e-mail: dahorsley@ucdavis.edu).

M. Li is with the Department of Electrical and Computer Engineering, University of California at Davis, Davis, CA 95616 USA (e-mail: moxli@ucdavis.edu).

E. Lasalandra is with the Analog, MEMS, Sensors Group, STMicroelectronics, Milan 20010, Italy (e-mail: ernesto.lasalandra@st.com).

Color versions of one or more of the figures in this paper are available online.

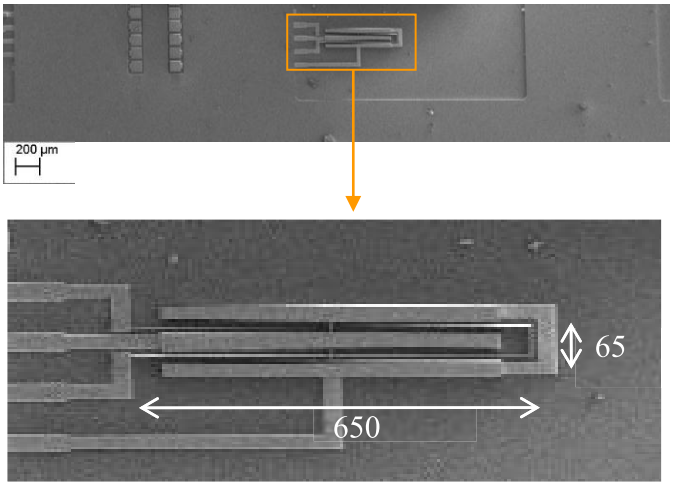

Fig. 1. SEM images of the experimentally tested resonating structure (dimensions in μm).

A simple, Lorentz force MEMS magnetometer fabricated with the industrial surface micromachining process THELMA of STMicroelectronics is discussed in the present paper. The fabricated device was tested in a laboratory under the action of a magnetic field generated by a coil. After a first design based on a trial-and-error approach, a collection of preliminary experimental results was obtained. Subsequently, the device dynamics was studied by means of an ad-hoc multi-physics model which takes into account, beside the Lorentz force contribution, the electrostatic loading due to capacitive sensing [10]–[12]. This approach allowed better design insights and the possibility to formulate a multi-physics, multi-constrained optimization approach similar to the one proposed in [11] and [12]. Optimality of the device geometry was then discussed making use of the multi-physics optimization algorithm.

The paper is organized as follows: in Section II the experimental results and sensor performance indexes obtained with the first designed and fabricated device are discussed. The multi-physics modelling is described in Section III. Optimization of the device geometry is presented and discussed in Section IV; while closing remarks are given in Section V.

II. Sensor Performance Indexes and Experimental Results

The newly designed device is shown in Fig. 1: its resonating structure is made of a single polysilicon structural layer, epitaxially grown over a single crystal silicon substrate.

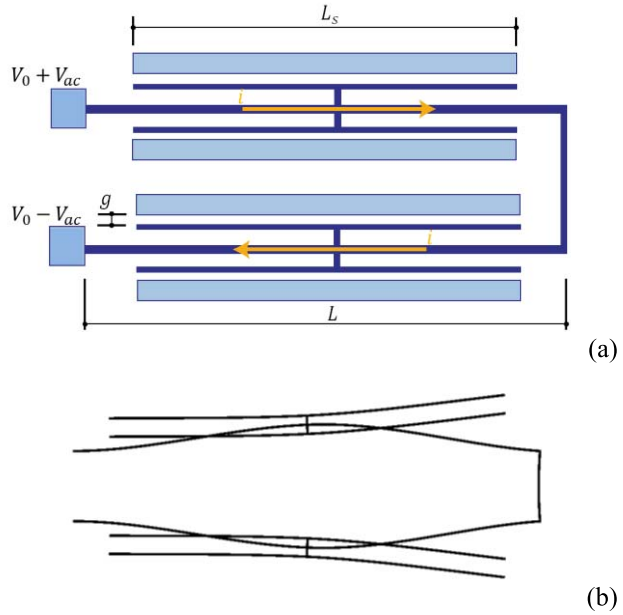

Fig. 2. (a) Device working principle and notation; (b) working vibration mode at resonance (displacements magnified 50 times).

Fig. 2 shows a schematic of the working principle of this device: a current i, flowing inside the suspended beams of length L, excites beam vibration under the action of a Lorentz force due to the presence of the out-of-plane external magnetic field. Sensing is achieved through two parallel plate capacitors of length L_s and gap g connected to the mid-span cross section, as shown in detail in Fig. 2a. The current flows thanks to the application of a bias voltage V_0 and AC voltage V_{ac}, as shown in Fig. 2.

The simplicity of the design and the reduced dimensions are the major features and improvements with respect to other designs proposed in the literature [2]–[9]. Moreover, possible parasitic sensitivity to in-plane acceleration is mechanically canceled, thanks to the symmetry of the structural design and to the differential sensing scheme, similar to the one presented in [2]. The cancellation is obtained as shown in Fig. 2b, where the working vibration mode of the sensor is depicted; this deformed configuration has been obtained with a finite element simulation, wherein all the beams have been modelled as Bernoulli-Euler ones due to their slenderness, i.e. to their high length/width ratio. The depicted mode shows that the two beams, composing the half Double-Ended Tuning Fork (DETF) structure, are moving anti-phase to each other, due to the opposite flow directions of the current i.

For characterization, the sensor was mounted on a printed circuit board with discrete electronics, as shown in Fig. 3; the simplified schematic of the electronic read-out circuit is given in Fig. 4. To generate the bias current inducing the Lorentz force, an AC current at the resonance frequency f of the DETF structure was injected on top of the DC bias voltage $V_0 = 3$ V. The bias current was 0.23 mA, which resulted in $V_{ac} = 1$ V voltage drop across the 8.5 kΩ current-carrying flexure. The power consumption due to the Lorentz force bias current was 0.24 mW, which could be much further reduced with a higher doping level of the structural layer. The resulting motion

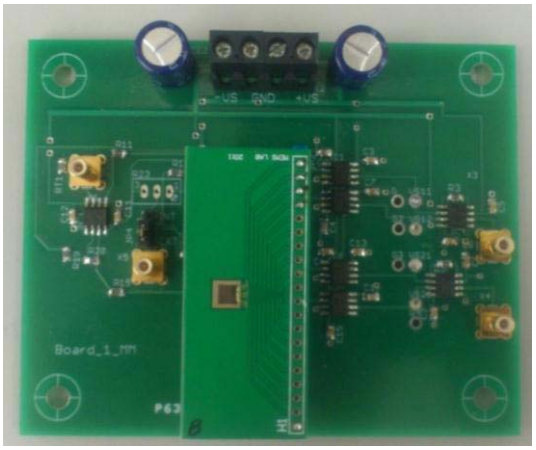

Fig. 3. Sensor mounted on a printed circuit board.

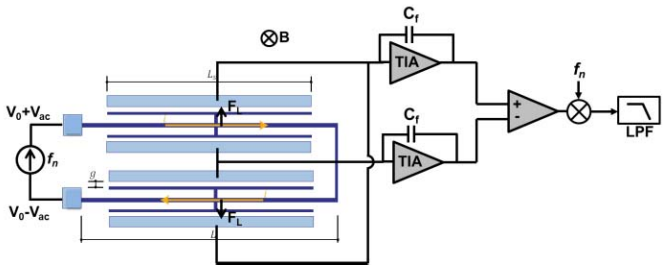

Fig. 4. Schematic of the readout circuit.

of the suspended beams was measured capacitively, using transimpedance amplifiers (TIA) with feedback capacitance $C_f = 1$ pF. The sensing current i generated by the capacitance pick-off, is given by:

$$i = V_0 \frac{dC}{dt} = V_0 \frac{C_0}{g} \dot{\mathcal{V}}, \tag{1}$$

where: $C_0 = 0.19$ pF is the reference value of the sensing capacitance C; $\mathcal{V}$ is the displacement of the moving sensing plates, which are assumed to undergo a purely translational rigid-body motion (see also the discussion in Section III); and g is the gap between the sensing plates, see Fig. 2a.

This current was then amplified by the transimpedance amplifier, whose output is given by:

$$V_{TIA} = V_0 \frac{C_0}{C_f} \frac{\mathcal{V}}{g}. \tag{2}$$

According to Eq. (2), a larger DC bias voltage V_0 or a smaller feedback capacitance C_f would result in a larger output signal. The differential signals from the two transimpedance amplifiers, as sketched in Fig. 4, passed through an instrumentation amplifier with a gain $G = 2$. The resulting signal was then demodulated and low-pass filtered to recover the magnetic signal back to baseband.

A single-axis Helmholtz coil was used to generate the testing magnetic field, with a maximum amplitude limited to 400 μT by the setup. To measure the frequency response of the device, the frequency of the bias current was swept from 19.2 kHz to 20.6 kHz, while a constant DC magnetic field was kept during the measurements. The measured frequency

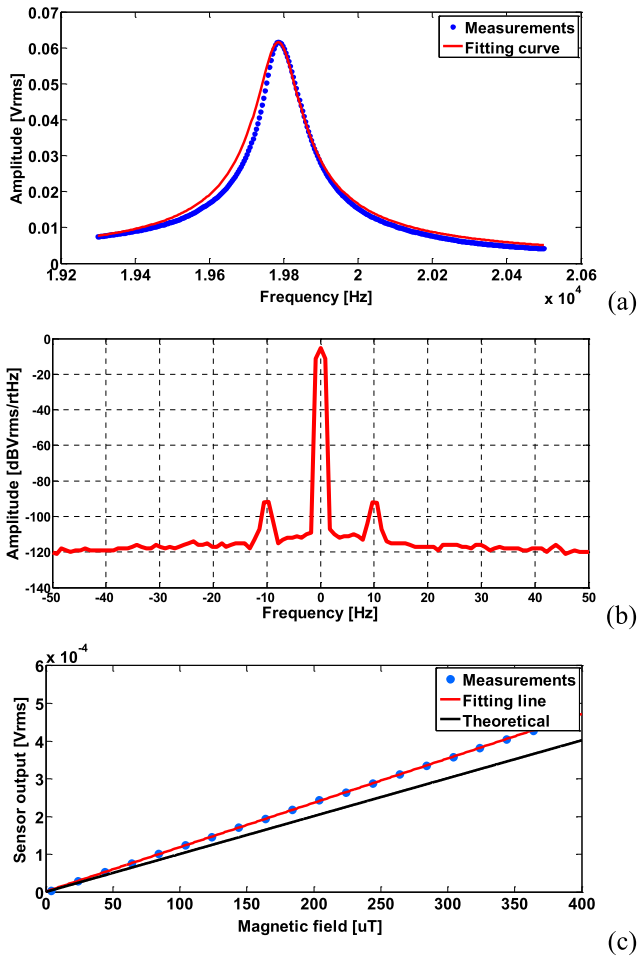

Fig. 5. (a) Frequency response of the sensor ($f = 19786$Hz, $Q = 164$); (b) output spectrum for in response to 10 Hz magnetic field input; (c) measured and theoretical magnetic transfer characteristic.

response, plotted in Fig. 5a, shows that the sensor has a resonance frequency $f = 19.8$ kHz. The response was then fitted to a second-order transfer function [2], and the fitted quality factor was $Q = 164$ and the 3 dB bandwidth of the sensor, $f/2Q$, was 60 Hz.

To separate the motion-current signal, Eq. (1), from the current resulting from capacitive feed-through of the excitation current at f, an AC magnetic field was applied with a frequency of 10 Hz. Fig. 5b shows the output spectrum, where the feed-through signal at carrier frequency f is centered at a frequency offset $\Delta f = 0$ Hz and the motion current signals at $\Delta f = \pm 10$ Hz indicate the response to the magnetic field input. Through tests conducted at varying magnetic field amplitudes, up to the aforementioned threshold of 400 μT, the device transfer characteristic was determined: the experimental output is compared with the relevant theoretical one in Fig. 5c. In this last plot, the discrepancy between the measurement and the theoretical sensitivity (see Section III) may be due to fabrication imperfections linked to e.g. over-etching; in fact, a smaller capacitive gap would result in larger sensitivity.

The resolution, in-plane dimensions, bandwidth and total mass of the vibrating structure of the proposed device are all compared in Table I with those of other similar Lorentz force magnetometers found in the recent literature, see [2]–[9].

TABLE I

COMPARISON OF PERFORMANCE INDEXES FEATURED BY CURRENT AND AVAILABLE LORENTZ FORCE MAGNETOMETERS

Publication	Axis	Resolution (nTmA/$\sqrt{\text{Hz}}$)	Dimensions (μm)	BW (Hz)	Total Mass (kg)
This work	Z	115	650×65	60	$5 \cdot 10^{-10}$
Li et al. [2]	X/Y	500	1080×800	69	$9.7 \cdot 10^{-9}$
Li et al. [3]	X/Y	88	200×1000	2.3	$8 \cdot 10^{-10}$
	Z	55	200×1000	7.4	
Li et. al. [4]	X	106	2000×2000	3.3	$5 \cdot 10^{-8}$
	Y	160	2000×2000	7.4	$5 \cdot 10^{-8}$
	Z	95	2000×2000	1.9	$5 \cdot 10^{-8}$
Thompson et al. [5]	Z	235	2000×1000	1	$6.8 \cdot 10^{-9}$
Kyynarainen* et al. [6]	Z	7	2000×400	2	$1.2 \cdot 10^{-9}$ **
Langfelder et al. [7]	Z	520	89×868	50	n.a.
Emmerich et al. [8]	Z	186	1300×500	1-10	$3.56 \cdot 10^{-9}$
Alandry et al. [9]	X/Y	1161	370×330	10	n.a.

*This device features an extra metal layer
**Estimated data

From data in Table I it can be remarked that the proposed sensor not only has the smallest area, but also provides a much larger bandwidth than other magnetometers with a similar resolution. In other words, it provides the most balanced key performance indexes; this is basically due to the small mass of the moving DETF structure.

Depending on the location, earth's magnetic field varies between 10 and 100 μT. Using 10 μT as a conservative estimate, the reported Brownian-noise-limited resolution of the sensor lies in the acceptable range for earth magnetic field detection and, therefore, navigation. Even if the sensor can be already judged very efficient, by optimizing the shape and size of the mechanical resonator, the overall device performance can be further enhanced. For instance, its bandwidth can be maximized without significantly reducing the sensitivity and resolution.

As mentioned, the preceding results were obtained with a bias voltage $V_0 = 3$ V. It should be mentioned that the pull-in voltage, amounting to $V_{pull-in} \approx 5$ V, limits the total voltage that can be applied to the device. This pull-in threshold could be improved by using comb-fingers instead of parallel plates for the capacitive sensing, but this would lead to lower device sensitivity.

III. MULTI-PHYSICS MODELING

As reported in Section I, the geometry of the experimentally tested device was arrived at through a trial-and-error structural optimization procedure, without considering all the performance indexes discussed in Section II. To further improve

a single performance index, or provide a balanced design keeping all the indexes into account, a structural optimization procedure will be discussed in Section IV. In this Section we instead focus on the multi-physics description of the device response to the applied magnetic field.

The two vibrating beams constituting the DETF structure are perfectly clamped at their left-ends. At their right-ends they are free to axially deform, so as to avoid effects of the axial force or residual stresses, see [12]; the beams are instead partially constrained in their in-plane bending due to the vertical, short connecting beam (shown in Fig. 2a). According to the resonance mode depicted in Fig. 2b, the effect of this connecting beam on the deformation of the horizontal ones is to almost prevent any rotation of the right-end cross sections. For ease of analysis, in what follows we thus disregard the beam compliance related to the aforementioned rotation. We therefore assume the horizontal beams to deform as if they had clamped-clamped boundary conditions.

Due to the symmetry of the resonating DETF structure, we focus now on a single beam having length L and constant cross section area A (see Fig. 2a). The elastic response of the beam to the external forces is modeled according to second-order theory, so as to account for lateral deflections affecting the equilibrium state. Dynamic equilibrium is enforced in weak form through (see also [13]):

$$\int_0^L \delta v'' E I v'' \mathrm{d}x + \int_0^L \delta v \eta \ddot{v} \mathrm{d}x - \int_0^L \delta v \, \not{f} \mathrm{d}x = 0, \qquad (3)$$

where shear deformations have been disregarded due to the high beam slenderness. In Eq. (3): $\delta \blacksquare$ stands for the variation of field $\blacksquare$; x is the coordinate along the longitudinal axis of the beam; $v(x)$ is the lateral beam displacement; $v'' = \partial^2 v / \partial x^2$ represents the curvature of the beam axis; $\ddot{v} = \partial^2 v / \partial t^2$, t being time, represents the lateral acceleration field; E is the effective Young's modulus of the beam material in the longitudinal direction, and EI is the flexural stiffness of the beam; $\eta = \rho A$ is the mass per unit length of the beam, ρ being the mass density of the beam material; $\not{f}$ is the magnitude of the external load per unit length.

As far as the external loading in Eq. (3) is concerned, the density $\not{f}$ is the sum of two terms: the electrostatic one $\not{f}_e$, and the Lorentz one $\not{f}_L$. According to what shown in Fig. 2a, where the beam and the attached sensing plates are held at the voltage $\hat{V}$ changing in time, and the sensing electrodes are held at $V = 0$, the term $\not{f}_e$ is given by:

$$\not{f}_e = \frac{1}{2} \hat{V}^2 \frac{\mathrm{d}C}{\mathrm{d}\mathcal{V}}, \qquad (4)$$

where: C is the capacitance per unit length between the beam and the two top and bottom electrodes; and $\mathcal{V}$ is the already discussed vertical displacement of the plates attached to the resonating beam, which are assumed to undergo a pure translational motion without tilting. While this assumption concerning the kinematics of the plate represents an approximation of the real vibration mode depicted in Fig. 2b, it is consistent with the symmetric beam deformation adopted in the model. As $\hat{V}$ results from the sum of a constant, bias term V_0 and of a co-sinusoidally varying term $V_{ac} = V_a \cos \omega t$, ω being the circular resonance frequency of the beam, we end up with:

$$\hat{V}^2 = V_0^2 + \frac{1}{2} V_a^2 + 2 V_0 V_a \cos[\omega t] + \frac{1}{2} V_a^2 \cos[2\omega t]. \qquad (5)$$

To compute $\mathrm{d}C/\mathrm{d}\mathcal{V}$ in Eq. (4), we now consider that the sensing plates do not deform at the system resonance in the proposed model; symmetry thus allows approximating the sensing system as two parallel-plate capacitors. Accounting for variations of the gap g between the moving plates and the sensing electrodes up to third-order terms in the displacement V, we get:

$$\frac{\mathrm{d}C}{\mathrm{d}\mathcal{V}} \cong \varepsilon_0 b \left(4 \frac{\mathcal{V}}{g^3} + 8 \frac{\mathcal{V}^3}{g^5} \right), \qquad (6)$$

where: ε_0 is the permittivity of vacuum; and b is the out-of-plane thickness of the beam and plates.

To clearly distinguish the response (and sensitivity) of the device to the two forces in Eq. (3), we consider that tests were carried out with a time-varying magnetic field B with circular frequency ω_B. Referring to the test results collected in Section II, ω_B is obviously related to Δf through $2\pi \, \Delta f = \omega_B$. This setup allows the last two terms of Eq. (5) to be omitted if the system response is monitored at $\omega \pm \omega_B$, instead of ω. Accordingly, the Lorentz force excitation f_L becomes:

$$f_L = \frac{i B_0}{2} \{ \cos[(\omega + \omega_B) t] + \cos[(\omega - \omega_B) t] \}, \qquad (7)$$

where B_0 stands for the maximum amplitude of the out-of-plane magnetic field.

With the aim of building a reduced-order model of the structure, we now assume the beam to vibrate according to its (linearized) resonance flexural mode, which features a lateral displacement v varying along x in accordance with:

$$v(x,t) = \frac{1}{2} \left(1 - cos \left(\frac{2\pi x}{L} \right) \right) \mathcal{V}(t), \qquad (8)$$

where, because of the assumed symmetry of deformation, $\mathcal{V}(t)$ represents the time history of the maximum lateral displacement experienced by the beam along x.

Besides the modeling of beam vibrations, we need to account for additional terms coming into play because of the attached sensing plates. These plates contribute to the mass of the system, which is:

$$m_a = 2 \eta^* L_s, \qquad (9)$$

where the factor of 2 accounts for the two plates attached to each beam and $\eta^* = \rho A^*$, A^* being the cross section area of each plate.

The plates also produce fluid damping, which is here assumed to be the dominant form of damping. In [1], we accounted for the damping force term derived from Reynolds equations. As the nominal working pressure of this sensor is 1 mbar, we instead consider here the energy transfer model for

squeeze-film air damping in low vacuum [14]. The relevant overall quality factor for a single beam is:

$$Q_{lv} = (2\pi)^{\frac{3}{2}} \rho b \omega \left(\frac{g}{2L_s}\right) \sqrt{\frac{RT}{M_m}} \frac{1}{p} \tag{10}$$

where, besides the variables already introduced, results depend on: the universal gas constant R; the working absolute temperature T; the molar weight of the air M_m; and the air pressure p. According to Eq. (10), in the low vacuum regime the quality factor Q_{lv} is inversely proportional to the air pressure p, which could be tuned to optimize the overall device performance. A difference between the model in [14] and Eq. (10) is that we have adopted $2L_s$ (see Fig. 2) to account for the two air films squeezed on the two sides of each beam while the DETF structure vibrates. This relation is valid provided that the Knudsen number Kn is large enough to fall in the free molecular flow regime, within which the collisions among gas molecules can be neglected. Obviously, if Kn is not large enough, the real quality factor might be smaller than that provided by Eq. (10).

By exploiting the assumed deformation mode (8) in the variational formulation (3) and by accounting for all the previously discussed terms, the motion of the beam can be described by the following ordinary differential equation:

$$m\ddot{\mathcal{V}} + d\dot{\mathcal{V}} + K_1 \mathcal{V} + K_3 \mathcal{V}^3 = \mathcal{F}(t), \tag{11}$$

where:

$$\begin{aligned} m &= \frac{3}{8}\eta L + 2\eta^* L_s \\ d &= \frac{\sqrt{K_1 m}}{Q_{lv}} \\ K_1 &= \frac{2\pi^4}{L^3} EI - 2\frac{\varepsilon_0 b L_s}{g^3}\left(V_0^2 + \frac{1}{2}V_a^2\right) \\ K_3 &= -4\frac{\varepsilon_0 b L_s}{g^5}\left(V_0^2 + \frac{1}{2}V_a^2\right) \\ F &= \frac{L}{4} i B_0 \left\{\cos\left[(\omega + \omega_B)t\right] + \cos\left[(\omega - \omega_B)t\right]\right\} \end{aligned} \tag{12}$$

respectively represent the effective mass, damping, linear and cubic stiffness, and external load terms.

Relation (11), which governs the dynamics of the beam vibrating according to its working resonance mode, is the well-known Duffing equation. In this equation, terms additional to those governing a standard linear oscillator are a result of the coupled electro-magneto-mechanical physics of the problem.

IV. Structural Optimization

In Section II, we have shown that the proposed device features good key performance indexes when compared to the best MEMS magnetometers found in the literature. Moreover, even if it does not provide the best resolution and bandwidth among those compared in Table I, it nevertheless features a well-balanced behavior that can be further improved.

In [1], we specifically focused on the Brownian-noise resolution. We optimized the geometry of the DETF structure to achieve high resolution, keeping (through ad-hoc constraints) a large bandwidth and a high sensitivity. In what follows, we provide a global optimization approach, dealing with multiple performance indexes simultaneously, within the frame of structural optimization.

TABLE II
Lower and Upper Bounds for the Set of Unknowns

	h (μm)	L (μm)	h_s (μm)	L_s (μm)	V_0 (V)
$\boldsymbol{\zeta}_m$	2	100	2	100	2
$\boldsymbol{\zeta}^M$	10	1000	10	1000	5

Overall, the goal of the optimization procedure is to minimize a scalar objective function defined as a weighted sum of the following performance indexes, see [3]: mechanical sensitivity φ_s (to be maximized); power consumption φ_p, linked to the electrical resistance of the DETF geometry (to be minimized); bandwidth φ_b (to be maximized); and resolution φ_r (to be minimized). The four indexes respectively read:

$$\begin{aligned} \varphi_s &= \frac{4\varepsilon_0 b L_s \mathcal{V}_{\max}}{g^2} \\ \varphi_p &= \frac{L}{A} \\ \varphi_b &= \frac{f}{2Q} \\ \varphi_r &= \frac{\sqrt{\frac{2}{\pi} T k_b \frac{K_1^*}{Qf^*}}}{L_E} \end{aligned} \tag{13}$$

where: $\mathcal{V}_{\max}$ is the maximum lateral displacement experienced by the mid-span cross section of the beam; k_b is the Boltzmann constant; K_1^* is the purely mechanical linear stiffness of the beam (i.e. $K_1^* = K_1(\hat{V} = 0)$); f^* is the relevant resonance frequency and L_E is the effective length of the current-carrying flexures.

To optimize the device, the DC bias voltage V_0 and the following geometrical parameters of the resonating structure are handled as unknowns in the relevant vector $\boldsymbol{\zeta}$, see Fig. 2a: the length L of the beam and its in-plane width h; the length L_s of the sensing plates and their in-plane width h_s. Suitable lower and upper bounds, respectively denoted with $\boldsymbol{\zeta}_m$ and $\boldsymbol{\zeta}^M$, are defined for the unknowns $\boldsymbol{\zeta}$, see Table II. The gap g is kept fixed at $g = 2$ μm, to guarantee that the fluid damping model providing Eq. (10) holds valid for any geometries compliant with $\boldsymbol{\zeta}_m \leq \boldsymbol{\zeta} \leq \boldsymbol{\zeta}^M$; this design parameter could be handled as an additional entry of the unknown vector $\boldsymbol{\zeta}$, but possible switches between different squeeze-film models would be required.

The resulting optimization problem may be framed according to:

$$\begin{cases} \min_{\boldsymbol{\zeta}} \varphi = -\beta_s \frac{\varphi_s}{\varphi_s} + \beta_p \frac{\varphi_p}{\varphi_p} - \beta_b \frac{\varphi_b}{\varphi_b} + \beta_r \frac{\varphi_r}{\varphi_r} \\ \text{s.t.} \\ \qquad f_m \leq f(\boldsymbol{\zeta}) \leq f^M \\ \qquad \boldsymbol{\zeta}_m \leq \boldsymbol{\zeta} \leq \boldsymbol{\zeta}^M \end{cases} \tag{14}$$

which also embeds the constraints f_m and f^M on the allowed resonance frequency of the structure. In the objective function of Eq. $(14)_1$, the minus signs obviously account for the fact that sensitivity and bandwidth have to be maximized while φ is

minimized. The four parameters $\beta_s, \beta_p, \beta_b, \beta_r$ allow assigning suitable weights to the relevant functions defined in Eq. (13). Due to the multi-physics of the problem at hand, the functions $\varphi_s, \varphi_p, \varphi_b, \varphi_r$ can take values in very different intervals (potentially differing by orders of magnitude); hence, the scaling factors $\bar{\varphi}_s, \bar{\varphi}_p, \bar{\varphi}_b, \bar{\varphi}_r$ are adopted in the formulation (14) to scale down or up the partial objective functions, and have them all comparable in amplitude. Algorithmically, the aforementioned scaling factors have been computed by first running four preliminary, uncoupled analyses, considering in Eq. $(14)_1$ only one partial objective function (through proper values of the weights, like e.g. $\beta_s = 1$ and $\beta_p = \beta_b = \beta_r = 0$): the value of the objective function at convergence of the algorithm has been then determined to be the scaling factor.

The two sets of constraints added to the formulation in (14) have different meanings. The one relevant to the design variables, usually referred to as side constraints, defines the feasible range for the optimization unknowns gathered in the vector $\boldsymbol{\zeta}$. The one relevant to the resonance frequency is instead introduced to guarantee that every optimal solution provides a working frequency of the device that is compliant with manufacturer's standard. In the numerical simulations presented next, it has been assumed that $f_m = 20$ kHz and $f^M = 30$ kHz.

The direct solution of the primary optimization problem (14) is not a trivial task, due to the computational burden tied to the evaluation of the nonlinear objective function and of the constraint functions, along with the relevant sensitivity analysis. To overcome this issue, the primary problem can be replaced with a sequence of explicit, approximate constrained sub-problems in the form:

$$\begin{cases} \min_{\boldsymbol{\zeta}} \tilde{\varphi} \\ \text{s.t.} \\ f_m \leq \tilde{f}(\boldsymbol{\zeta}) \leq f^M \\ \boldsymbol{\zeta}_m \leq \boldsymbol{\zeta} \leq \boldsymbol{\zeta}^M \end{cases} \tag{15}$$

where $\tilde{\varphi}$ and $\tilde{f}$ may be seen as Taylor series expansions of the objective function φ and the frequency function f around the current design point. The sub-problems arising in (15) can be efficiently handled through mathematical programming algorithms that are based on the so-called dual methods, like the herein adopted method of moving asymptotes, MMA [15]. Dual methods extensively exploit convexity and separability properties of the sub-problems in (15). The convexity of the approximation ensures that the solution of the dual problem is the same of the original one. The separability allows deriving an uncoupled system of equations between the primal variables and the dual unknowns, meaning that the problem can be solved independently for each primal variable.

MMA looks for the optimal solution while robustly enforcing the constraints throughout the optimization procedure. Unknowns are also scaled during the analysis, before entering the minimization, in order to ensure compliance with the feasible domain boundaries for each optimization unknown in $\boldsymbol{\zeta}$.

With the aim of computing the scaling factors in Eq. (14) and to start validating the adopted procedure, a set of investigations has been first performed by handling only one partial objective function in turn. The outcomes relevant to this uncoupled optimization are summarized in Table III, where each row refers to an optimization run handling the performance index listed in leftmost column. The final performance achieved through the optimal design is reported in terms of sensitivity φ_s, power consumption φ_p, bandwidth φ_b and resolution φ_r.

TABLE III
UNCOUPLED OPTIMIZATION: OPTIMAL DESIGNS AND RELEVANT PERFORMANCE INDEXES

Perf. index	h (μm)	L (μm)	h_s (μm)	L_s (μm)	V_0 (V)	φ_s $\left(\frac{\text{fF}}{\text{T}}\right)$	φ_p (μm^{-1})	φ_b (Hz)	φ_r $\left(\frac{\text{nTmA}}{\sqrt{\text{Hz}}}\right)$
φ_s	2	797	2	100	2	98.8	18.1	13.4	26
φ_p	9.1	1000	10	1000	5	4.97	5.01	134	304
φ_b	4.6	679	6.3	1000	3.5	6.71	6.67	134	347
φ_r	2.8	1000	2	100	2	89.3	16.2	13.4	25

Table III shows that each optimization run provides a design whose relevant performance index is better than all the others achieved considering different target indexes. Due to the nonlinearity of the problem, multiple optimal solutions can occur: for instance, the two solutions providing maximum sensitivity and minimum resolution share the same h_s and L_s values, and also the same bandwidth. Something similar holds true for the optimal solutions governed by the minimum power consumption and maximum bandwidth. It is worth noting that the optimal solutions maximizing the sensitivity or minimizing the resolution have been attained along the lower bound constraint on the resonance frequency; conversely, the optimal designs minimizing the power consumption has been attained at the upper bound on the resonance frequency.

The three solutions related to the optimization of φ_s, φ_p and φ_r have been obtained independently of the starting point, thus proving to be unique. The other way around, a set of optimal designs has been found while maximizing the bandwidth φ_b; this is strictly related to the possibility of multiple optimal solutions encountered when dealing with nonlinear problems.

Besides the already discussed values of some optimization unknowns shared by the optimal designs at convergence, it must be noted that the constrained minimization of the power consumption is attained for the upper bounds on L, L_s, h_s and V_0, while the remaining unknown h is close to its upper bound. The optimal design that maximizes the sensitivity is completely different, with h, L_s, h_s and V_0 at their minimum allowed values, while L is governed by one bound on the resonance frequency. This optimal layout is not much different from the one achieved to maximize the resolution.

Moving now to the complete, or coupled optimization solution, where all the performance indexes are dealt with together, Table IV gathers the design parameters providing the minimum of the objective function φ in Eq. $(14)_1$ when $\beta_s = \beta_p = \beta_b = \beta_r = 1$, i.e. for a balanced performance of the device. As large values of L improve all the performance indexes, see Table III, the reported design's value is the maximum allowed. As the other unknowns affect each index differently, no clues can be obtained from Table III; looking

TABLE IV
COUPLED OPTIMIZATION: OPTIMAL DESIGN AND RELEVANT PERFORMANCE INDEXES ACHIEVED FOR $\beta_s = \beta_p = \beta_b = \beta_r = 1$

h (μm)	L (μm)	h_s (μm)	L_s (μm)	V_0 (V)	φ_s $\left(\frac{\text{fF}}{\text{T}}\right)$	φ_p (μm^{-1})	φ_b (Hz)	φ_r $\left(\frac{\text{nTmA}}{\sqrt{\text{Hz}}}\right)$
4	1000	2	100	5	46.5	11.3	13.4	28

at the outcome in Table IV, it turns out that all the entries of $\boldsymbol{\zeta}$ but h belong to one side constraint.

Needless to say, the current solution is tightly linked to the selected values of the weights; as already reported in [11] for a simpler sensor geometry, a different set of weights might induce switches among competing optimal designs, or even a smooth transition from one to another.

The values of the individual performance indexes reported in Table IV are not as good as those in Table III, where they have been considered one by one in the optimization procedure. Accordingly, looking at the values of all the indexes it can be seen that this coupled optimization provides the most balanced behavior of the device; this is due to the assumed common value of all the weights. Eventually, it has to be remarked that the obtained optimal design features the maximum allowed resonance frequency, i.e. $f = f^M = 30$ kHz.

As previously discussed, MMA is an iterative method searching for the optimal values of the unknowns in $\boldsymbol{\zeta}$ that minimize φ and fulfill constraints of the type $f_m \leq f(\boldsymbol{\zeta}) \leq f^M$. This set of two constraints can be equivalently read in a non-dimensional form, as an upper bound inequality $f(\boldsymbol{\zeta})/f^M \leq 1$ and a lower bound inequality $f(\boldsymbol{\zeta})/f_m \geq 1$. With a straightforward manipulation, the latter can be re-written as $-f(\boldsymbol{\zeta})/f_m \leq -1$, or $-f(\boldsymbol{\zeta})/f_m + 2 \leq 1$: these non-dimensional forms allow confirmation within a common formalism whether they are satisfied by the current solution of the iterative procedure. To this aim, the maximum between the two ratios $f(\boldsymbol{\zeta})/f_m$ and $-f(\boldsymbol{\zeta})/f_m + 2$ is defined as the feasibility of the constraint: when this index converges toward a unitary value, it means that the final solution leads to a resonance frequency belonging to the border of the feasible, or allowed, domain; whereas when it converges toward a value lower than one, it means that the optimal solution features a resonance frequency within the allowed domain.

Due to the nonlinear objective function considered here, local minima of φ can provide sub-optimal solutions. To avoid this, according to a rather standard procedure, we have adopted different initialization points of the iterative procedure, sometimes even not compliant with all the constraints. Values of the objective function attained at each intermediate step of the optimization procedure can then be collected in a history plot, to check for convergence toward the sought global minimum; if this does not occur, the corresponding solution (sub-optimal, as stated here above) is disregarded.

Figure 6 shows the evolution of φ for three different (exemplary) initializations of $\boldsymbol{\zeta}$, randomly chosen in the allowed domain. It can be seen that all the runs ended with a plateau

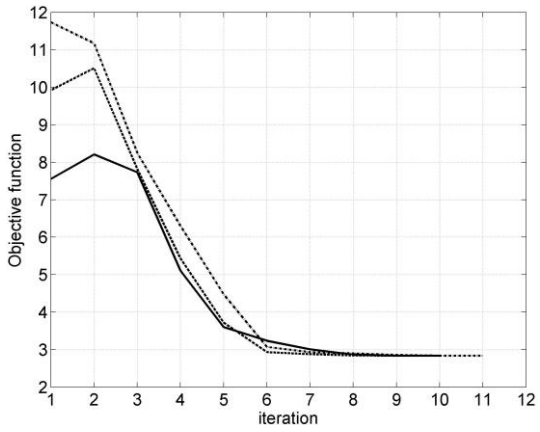

Fig. 6. History plot of the objective function φ for different starting guesses.

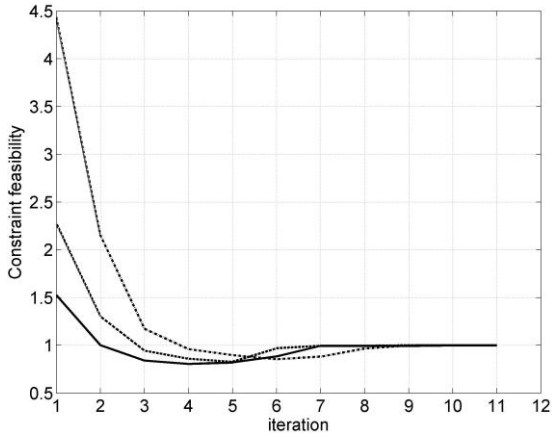

Fig. 7. History plot of the constraint feasibility for different starting guesses.

featuring the same value of the objective function; this means that a smooth convergence to the global minimum has been found. Figure 7 shows instead the relevant evolutions of the aforementioned constraint feasibility. Such results testify that in the first iterations, the algorithm tries the enforcement of full constraint feasibility, possibly leading to an increasing value of the objective function. Once constraints are appropriately fulfilled, the minimization of φ is performed efficiently, with fast convergence towards an optimal and fully feasible design.

All the above results thus support our claim regarding the robustness of the methodology, the convergence toward the global minimum of the objective function (since it always has the same final value), the good convergence rate (due to the limited number of iterations and the smooth history plots), and the full feasibility of the solution (as constraints are always satisfied at convergence), see also [16].

V. CONCLUSIONS

A z-axis Lorentz-force micro magnetic field sensor was designed, fabricated and tested. The proposed device combines efficiency and reduced dimensions, keeping a good balance between the considered key performance indexes and very small dimensions. The sensor could be used for out-of-plane earth magnetic field detection in consumer market compasses. A multi-physics formulation was adopted to model the sensor output and multi-physics, multi-objective parameter

optimization strategies were formulated and applied for the device optimization. The obtained results can be exploited as the basis for possible alternative designs.

ACKNOWLEDGMENT

The contribution of A. Tocchio and H. Najar for device design and measurements is gratefully acknowledged.

REFERENCES

[1] M. Bagherinia, A. Corigliano, S. Mariani, D. A. Horsley, M. Li, and E. Lasalandra, "An efficient earth magnetic field MEMS sensor: Modelling and experimental results," in *Proc. IEEE 27th Int. Conf. MEMS*, San Francisco, CA, USA, Jan. 2014, pp. 700–703.

[2] M. Li, V. T. Rouf, G. Jaramillo, and D. A. Horsley, "MEMS Lorentz force magnetic sensor based on a balanced torsional resonator," in *Proc. 17th Int. Conf. TRANSDUCERS*, Barcelona, Spain, Jun. 2013, pp. 66–69.

[3] M. Li, V. T. Rouf, M. J. Thompson, and D. A. Horsley, "Three-axis Lorentz-force magnetic sensor for electronic compass applications," *J. Microelectromech. Syst.*, vol. 21, no. 4, pp. 1002–1010, Aug. 2012.

[4] M. Li *et al.*, "Single-structure 3-axis Lorentz force magnetometer with sub-30 nT/$\sqrt{}$HZ resolution," in *Proc. IEEE 27th Int. Conf. MEMS*, San Francisco, CA, USA, Jan. 2014, pp. 80–83.

[5] M. J. Thompson and D. A. Horsley, "Parametrically amplified Z-axis Lorentz force magnetometer," *J. Microelectromech. Syst.*, vol. 20, no. 3, pp. 702–710, Jun. 2011.

[6] J. Kyynäräinen *et al.*, "A 3D micromechanical compass," *Sens. Actuators A, Phys.*, vol. 142, no. 2, pp. 561–568, 2008.

[7] G. Langfelder, C. Buffa, A. Frangi, A. Tocchio, E. Lasalandra, and A. Longoni, "Z-axis magnetometers for MEMS inertial measurement units using an industrial process," *IEEE Trans. Ind. Electron.*, vol. 60, no. 9, pp. 3983–3990, Sep. 2013.

[8] H. Emmerich and M. Schofthaler, "Magnetic field measurements with a novel surface micromachined magnetic-field sensor," *IEEE Trans. Electron Devices*, vol. 47, no. 5, pp. 972–977, May 2000.

[9] B. Alandry, L. Latorre, F. Mailly, and P. Nouet, "A fully integrated inertial measurement unit: Application to attitude and heading determination," *IEEE Sensors J.*, vol. 11, no. 11, pp. 2852–2860, Nov. 2011.

[10] L. Chen, W. Wang, Z. Li, and W. Zhu, "Stationary response of Duffing oscillator with hardening stiffness and fractional derivative," *Int. J. Non-Linear Mech.*, vol. 48, pp. 44–50, Jan. 2013.

[11] A. Corigliano, M. Bagherinia, M. Bruggi, S. Mariani, and E. Lasalandra, "Optimal design of a resonating MEMS magnetometer: A multi-physics approach," in *Proc. 14th Int. Conf. EuroSimE*, Wrocław, Poland, Apr. 2013, no. 6529931, pp. 1–6.

[12] M. Bagherinia, M. Bruggi, A. Corigliano, S. Mariani, and E. Lasalandra, "Geometry optimization of a Lorentz force, resonating MEMS magnetometer," *Microelectron. Rel.*, vol. 54, nos. 6–7, pp. 1192–1199, 2014.

[13] X. Xi, Z. Yang, L. Meng, and C. Zhu, "Primary resonance of the current-carrying beam in thermal-magneto-elasticity field," *Appl. Mech. Mater.*, vols. 29–32, pp. 16–21, Aug. 2010.

[14] M. Bao and H. Yang, "Squeeze film air damping in MEMS," *Sens. Actuators A, Phys.*, vol. 136, no. 1, pp. 3–27, 2007.

[15] K. Svanberg, "The method of moving asymptotes—A new method for structural optimization," *Int. J. Numer. Methods Eng.*, vol. 24, no. 2, pp. 359–373, 1987.

[16] M. Bruggi and S. Mariani, "Optimization of sensor placement to detect damage in flexible plates," *Eng. Optim.*, vol. 45, no. 6, pp. 659–676, 2013.